2021 43rd Annual International Conference of the
IEEE Engineering in Medicine & Biology Society (EMBC)
Oct 31 - Nov 4, 2021. Virtual Conference

Slant-Stack Migration Applied to Plane-Wave Ultrasound Imaging

Daler Rakhmatov

***Abstract*— Ultrafast plane-wave ultrasound imaging replaces numerous focused-beam transmissions with a single emitted plane-wave pulse, insonifying the entire subsurface region of interest all at once. To improve image quality, one can employ coherent plane wave compounding (CPWC), whereby several pulses are emitted sequentially at different steering angles, and their corresponding acquired raw data frames are individually beamformed and then combined to form a final reconstructed image frame. We describe a classic geophysical reconstruction technique called slant-stack migration, adapted here to CPWC imaging. Our evaluation results, based on two public-domain datasets featuring both anechoic and hyperechoic targets, demonstrate that the presented approach compares favorably with conventional delay-and-sum beamforming.**

***Clinical relevance*— Plane-wave ultrasound imaging allows for raw data acquisitions at very high frame rates, thus enabling accurate characterization of fast dynamics of blood or tissue motion. High quality of CPWC images reconstructed from raw data contributes to making appropriate clinical decisions.**

I. INTRODUCTION

Plane-wave ultrasound imaging, where a few plane-wave emissions replace a multitude of focused-beam transmissions, makes it possible to acquire raw data frames at a very high rate. It offers increased temporal resolution, which enhances ultrasound-based diagnostic capabilities in such areas as Doppler imaging and shear-wave elastography [1]. Typically, one uses several plane-wave pulses emitted at different steering angles, which yields several raw data frames. They are individually beamformed, and then their corresponding complex-valued beamformed frames are combined to obtain a final reconstructed image frame. This process is known as *coherent plane wave compounding* (CPWC) [2].

The focus of this work is on CPWC image reconstruction using so-called *slant-stack migration*, a technique originating from the geophysical literature (e.g., see [3]). It has been adapted here to plane-wave data processing as a viable alternative to conventional delay-and-sum (DAS) beamforming.

The original slant-stack migration method relies on the 2D scalar wave equation

$$\left[\frac{\partial^2}{\partial x^2}+\frac{\partial^2}{\partial z^2}\right]P(t,z,x)=\frac{1}{\widehat{v}^2}\frac{\partial^2}{\partial t^2}P(t,z,x), \qquad (1)$$

where t represents time, $P(t,z,x)$ is the wavefield in 2D spatial coordinates z (axial) and x (lateral), and $\widehat{v}=c/2$ is a one-way propagation velocity that arises from the *exploding reflector model* (ERM) setting [3], [4]. The latter means that we ignore the downgoing pulse propagation delays from the surface transmitters (located at $z=0$) to some reflector at depth $z>0$, and instead let the upgoing echoes from that reflector travel back to the surface receivers at half-speed $c/2$. Then, we can assume that reflectors "explode" at time $t=0$, forming a wavefield described by (1). The resulting signals (i.e., received echoes caused by a transmitted pulse) are recorded as $P(t,0,x)$ by the surface receivers along the x-axis. Given a raw dataset $P(t,0,x)$, the goal of migration is to reconstruct an image dataset $P(0,z,x)$, revealing a 2D reflectivity map of the insonified medium section.

We have the following classic result (e.g., see [3], [4]):

$$P(0,z,x)=\iint\limits_{\widehat{v}^2k_x^2<f^2}\Psi(f,0,k_x)e^{j2\pi(k_z z+k_x x)}df\,dk_x, \qquad (2)$$

where $k_z=(f/\widehat{v})\sqrt{1-(\widehat{v}k_x/f)^2}$ subject to $\widehat{v}^2k_x^2<f^2$, and $\Psi(f,0,k_x)$ is the Fourier transform of $P(t,0,x)$ with respect to t and x. Introducing the *slant* parameter $p_x=k_x/f$ yields

$$P(0,z,x)=\iint\limits_{\widehat{v}^2p_x^2<1}|f|\Psi(f,0,fp_x)e^{j2\pi f\tau(z,x,p_x)}df\,dp_x, \qquad (3)$$

where $\tau(z,x,p_x)=p_x x+(z/\widehat{v})\sqrt{1-(\widehat{v}p_x)^2}$ subject to $\widehat{v}^2p_x^2<1$. Next, we note that

$$\Psi(f,0,fp_x)=\int\Phi(f,0,x)e^{-j2\pi fp_x x}dx, \qquad (4)$$

where $\Phi(f,0,x)$ is the Fourier transform of $P(t,0,x)$ with respect to t. Finally, we let

$$\overline{\Phi}(t,0,p_x)=\int|f|\Psi(f,0,fp_x)e^{j2\pi ft}df \qquad (5)$$

and obtain

$$P(0,z,x)=\int\limits_{\widehat{v}^2p_x^2<1}\overline{\Phi}(\underbrace{p_x x+(z/\widehat{v})\sqrt{1-(\widehat{v}p_x)^2}}_{t=\tau(z,x,p_x)},0,p_x)dp_x. \qquad (6)$$

In other words, computing $P(0,z,x)$ involves interpolating $\overline{\Phi}(t,0,p_x)$ along the t-axis using $\tau(z,x,p_x)$ and then integrating over p_x (slant stacking).

The next section describes how one can modify slant-stack migration outlined above, so that it can be used for CPWC image reconstruction. We let θ denote the steering angle of a plane-wave pulse, and in the sequel, we attach subscript θ to all symbols representing angle-dependent quantities (P_θ, Ψ_θ, Φ_θ, $\overline{\Phi}_\theta$, τ_θ).

This work was supported in part by the Natural Sciences and Engineering Research Council of Canada (NSERC).

The author is with the Department of Electrical and Computer Engineering (ECE), University of Victoria, Victoria B.C., Canada V8P 5C2 daler@ece.uvic.ca

II. PROPOSED METHODS

Fig. 1 provides a simple geometric illustration of the main idea behind our proposed methods. When the transmitted pulse wavefront W^* reaches a reflector R located at some (z,x) coordinates, R "explodes", thus generating an echo signal that travels back to the surface (see Fig. 1). We assume that the echo propagation velocity is c (the speed of sound in the imaged medium), as opposed to $\widehat{v} = c/2$. Consequently, the transmitted pulse propagation delay can no longer be ignored and must be accounted for explicitly.

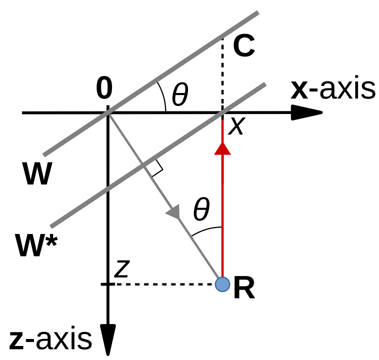

Fig. 1. Geometric illustration.

Since the travel distance between W^* and R is $z\cos(\theta)$, the pulse delay in question equals $z\cos(\theta)/c$, which can be accounted for by introducing the corresponding phase shift $\exp(j2\pi f z\cos(\theta)/c)$. As a result, we get new

$$\tau_\theta(z,x,p_x) = p_x x + (z/c)\left[\cos(\theta) + \sqrt{1-(cp_x)^2}\right]. \quad (7)$$

We still need additional modifications, as the true transmitted pulse wavefront is W (crossing $x=0$ in Fig. 1), i.e., not W^* aligned with the x-coordinate of R. Hence, we consider two options: 1) applying depth corrections *after* slant stacking, or 2) introducing additional delays *before* slant stacking.

The first option implies interpolating $\overline{\Phi}_\theta(t,0,p_x)$ using $t = \tau_\theta(z,x,p_x)$ given by (7). Subsequent integration over p_x produces $P_\theta(0,\bar{z},x)$, where the preliminary $\bar{z}$-coordinates of reflectors must be corrected to their true z-coordinates. As $z = ct/2$, the corresponding depth adjustments are given by $\Delta z = c\Delta t/2$, where $c\Delta t = x\tan(\theta)$ is the extra travel distance between points $(0,x)$ and C (see Fig. 1). Thus, we have $z = \bar{z} + x\tan(\theta)/2$. The resulting plane-wave slant-stack migration method, abbreviated as PWSSa, is outlined below.

PWSS*a* Method

1. Compute $\Phi_\theta(f,0,x)$ by applying the 1D Fourier transform to $P_\theta(t,0,x)$ with respect to t. Select a set of p_x values subject to $c^2p_x^2 < 1$. Initialize $P_\theta(0,\bar{z},x) \leftarrow \mathbf{0}$.
2. For each p_x perform the following two steps:
i) Multiply $\Phi_\theta(f,0,x)$ by $\exp(-j2\pi f p_x x)$ and sum over x. Multiply the result by $|f|$ and then apply the 1D inverse Fourier transform with respect to f, which yields $\overline{\Phi}_\theta(t,0,p_x)$.
ii) For each x, compute $\tau_\theta(z,x,p_x)$ using (7). Determine $\overline{\Phi}_\theta(\tau_\theta(z,x,p_x),0,p_x)$ and add it to $P_\theta(0,\bar{z},x)$.
3. Let $P_\theta(0,z,x) \leftarrow P_\theta(0,\bar{z}+x\tan(\theta)/2,x)$.

The second option implies introducing an additional phase shift $\exp(j2\pi f x\sin(\theta)/c)$, where $x\sin(\theta)/c$ represents the propagation delay between the pulse wavefronts W and W^* (see Fig. 1). Consequently, we obtain adjusted

$$\tau'_\theta(z,x,p_x) = x\sin(\theta)/c + \tau_\theta(z,x,p_x), \quad (8)$$

to be used when interpolating $\overline{\Phi}_\theta(t,0,p_x)$ prior to integration over the slant variable p_x. The resulting plane-wave slant-stack migration method, abbreviated as PWSSb, is outlined below.

PWSS*b* Method

1. Compute $\Phi_\theta(f,0,x)$ by applying the 1D Fourier transform to $P_\theta(t,0,x)$ with respect to t. Select a set of p_x values subject to $c^2p_x^2 < 1$. Initialize $P_\theta(0,z,x) \leftarrow \mathbf{0}$.
2. For each p_x perform the following two steps:
i) Multiply $\Phi_\theta(f,0,x)$ by $\exp(-j2\pi f p_x x)$ and sum over x. Multiply the result by $|f|$ and then apply the 1D inverse Fourier transform with respect to f, which yields $\overline{\Phi}_\theta(t,0,p_x)$.
ii) For each x, compute $\tau'_\theta(z,x,p_x)$ using (8). Determine $\overline{\Phi}_\theta(\tau_\theta(z,x,p_x),0,p_x)$ and add it to $P_\theta(0,z,x)$.

The asymptotic complexity of both PWSSa and PWSSb methods, dominated by step **2**, is $O(n_t n_x n_p)$ per angle θ, where n_p is the number of slants in use, and $n_t \times n_x$ is the size of the 2D input $P_\theta(t,0,x)$.

It is important to mention that PWSSa closely resembles another slant-stack method reported in our earlier work [5]. We briefly discuss their relationship in the next section that presents our evaluation results.

III. EVALUATION RESULTS

To assess the slant-stack migration methods described in the previous section, we have used two experimental datasets provided by the PICMUS evaluation framework [6], [7]. This framework also provides a reference implementation of conventional DAS beamforming with different apodization windows – we have used two of them: Tukey-25% (with the 1/4 cosine fraction) and Boxcar. These baseline beamformers are referred to as DAS_1 and DAS_2, respectively.

The first dataset, labeled TYPE-1, features two anechoic cyst targets and one hyperechoic wire target. The second dataset, labeled TYPE-2, features seven hyperechoic wire targets. In both cases, the raw datasets are of size 1536×128, while the reconstructed image datasets are of size 1536×384 (i.e., upsampled by the factor of 3 along the x-axis). Examples of the TYPE-1 and TYPE-2 CPWC B-mode images obtained using DAS_1 are shown in Fig. 2 and Fig. 3.[1] For

[1] The dynamic range of all displayed B-mode images is 60 dB.

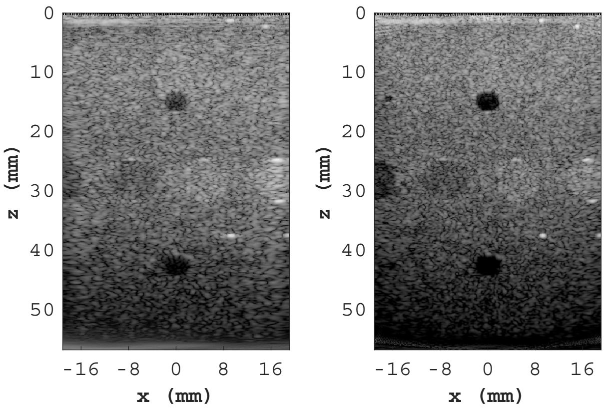

Fig. 2. TYPE-1 CPWC images, DAS_1: 1 PW (left), 19 PWs (right).

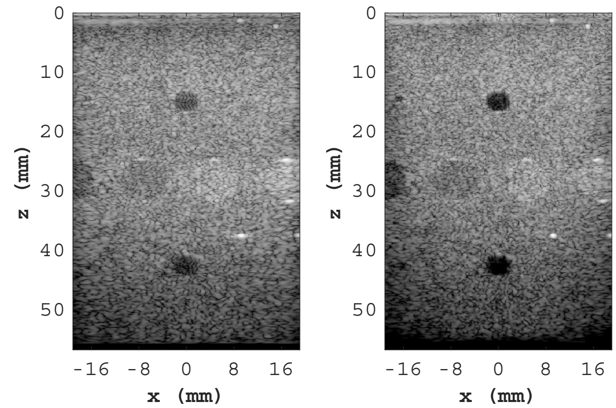

Fig. 4. TYPE-1 CPWC images, $\text{PWSS}b_1$: 1 PW (left), 19 PWs (right).

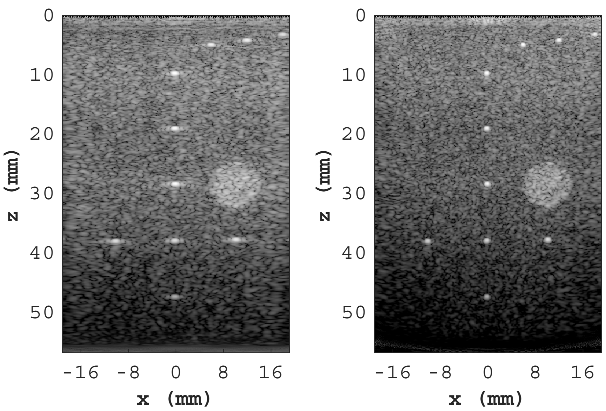

Fig. 3. TYPE-2 CPWC images, DAS_1: 1 PW (left), 19 PWs (right).

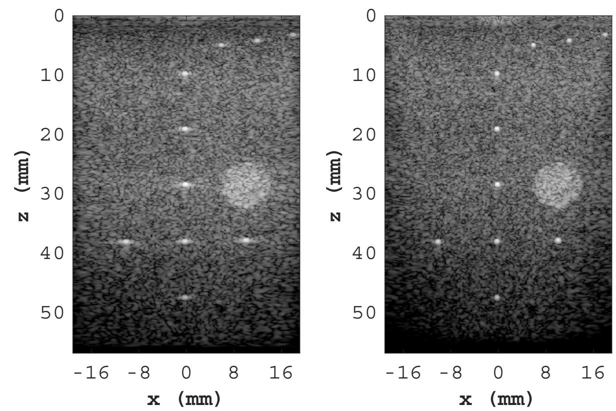

Fig. 5. TYPE-2 CPWC images, $\text{PWSS}b_1$: 1 PW (left), 19 PWs (right).

evaluation purposes, we have considered two representative cases: 1) a single plane-wave emission having $\theta = 0°$ (left-side images), and 2) nineteen plane-wave emissions having uniformly spaced θ values from $-16°$ to $+16°$ (right-side images).

In addition to DAS_1 and DAS_2, we compare the performance of our PWSSa and PWSSb methods with[2]

- Temme-Mueller migration [12], referred to as TM,[3]
- Modified Stolt's migration from section IV.A of [5], referred to as method A,
- Modified slant-stack migration from section IV.B of [5], referred to as method B.

For PWSSa, PWSSb, and B, we have used the slant spacing $\Delta p_x = 1/(f_{\text{max}} n_x \Delta x)$, where Δx is the transducer element spacing, and f_{max} is the maximum frequency of our Fourier grid. As for the number of slants, we have considered two settings: 1) $n_p = 130$, generating $p_x \in [-0.3/c, +0.3/c]$ (used in $\text{PWSS}a_1$, $\text{PWSS}b_1$, and B_1), and 2) $n_p = 260$, generating $p_x \in [-0.5/c, +0.5/c]$ (used in $\text{PWSS}a_2$, $\text{PWSS}b_2$, and B_2). Examples of the TYPE-1 and TYPE-2 CPWC B-mode images obtained using $\text{PWSS}b_1$ are shown in Fig. 4 and Fig. 5.

[2]Other representative works, such as [8]–[11], are not covered here. Their key features and relative performance are discussed extensively in [5].

[3]It appears that Temme-Mueller migration have been overlooked in the ultrasound literature. This method is evaluated here for the first time.

Our performance evaluations rely on the following PICMUS image quality indicators [6]:

- *Contrast-to-noise ratio* (CNR) values, associated with the two anechoic cyst targets that appear as dark disks in the TYPE-1 images,
- *Full-width at half-maximum* (FWHM) values, associated with the hyperechoic wire targets that appear as bright points the TYPE-1 (one near the bottom cyst) and TYPE-2 (seven in a cross-shaped alignment) images.

Tables I and II list our measurements, where $\overline{\text{FWHM}}$ denotes the FWHM values averaged over all seven wire targets under consideration in the TYPE-2 images. It should be noted that in the special case of a single plane-wave emission (i.e., for $\theta = 0°$), the migration equations of methods TM and A become identical, thus producing identical results; the same is true for methods PWSSa, PWSSb, and B.

In Table I, methods TM and A offer the best $\text{CNR}_{\text{Top}} = 8.6$ dB for the top cyst as well as the best $\text{CNR}_{\text{Bottom}} = 7.6$ dB for the bottom cyst. The same $\text{CNR}_{\text{Bottom}}$ is also produced by methods $\text{PWSS}a_2$, $\text{PWSS}b_2$, and B_2. These three methods yield the best $\text{FWHM}_{\text{Lateral}}$ (measured horizontally along the x-axis), equal to 0.805 and 0.748 mm for the TYPE-1 and TYPE-2 images, respectively. Methods TM and A produce the best $\text{FWHM}_{\text{Axial}}$ (measured vertically along the z-axis), equal to 0.487 and 0.486 mm for the TYPE-1 and TYPE-2 images, respectively.

TABLE I

IMAGE QUALITY INDICATORS: SINGLE PLANE WAVE, $\theta = 0°$.

Method	TYPE-1 Top/Bottom CNR (dB)	TYPE-1 Axial/Lateral FWHM (mm)	TYPE-2 Axial/Lateral $\overline{\text{FWHM}}$ (mm)
DAS_1 [6]	$8.4/7.1$	$\mathbf{0.487}/0.970$	$0.488/0.962$
DAS_2 [6]	$7.6/6.1$	$\mathbf{0.487}/0.902$	$0.490/0.876$
TM [12], A [5]	$\mathbf{8.6}/\mathbf{7.6}$	$\mathbf{0.487}/0.844$	$\mathbf{0.486}/0.791$
B_1 [5], $\text{PWSS}a_1$, $\text{PWSS}b_1$	$8.2/6.8$	$0.494/0.863$	$0.489/0.791$
B_2 [5], $\text{PWSS}a_2$, $\text{PWSS}b_2$	$7.8/\mathbf{7.6}$	$0.491/\mathbf{0.805}$	$0.490/\mathbf{0.748}$

TABLE II

IMAGE QUALITY INDICATORS: 19 PLANE WAVES, $\theta \in [-16°, +16°]$.

Method	TYPE-1 Top/Bottom CNR (dB)	TYPE-1 Axial/Lateral FWHM (mm)	TYPE-2 Axial/Lateral $\overline{\text{FWHM}}$ (mm)
DAS_1 [6]	$13.1/11.5$	$\mathbf{0.487}/0.630$	$0.486/0.603$
DAS_2 [6]	$12.8/11.5$	$\mathbf{0.487}/0.601$	$0.486/0.578$
TM [12]	$11.0/11.8$	$0.491/0.543$	$0.490/0.518$
A [5]	$12.5/\mathbf{12.2}$	$\mathbf{0.487}/0.504$	$\mathbf{0.482}/\mathbf{0.463}$
B_1 [5]	$13.2/11.1$	$0.491/0.582$	$0.487/0.549$
$\text{PWSS}a_1$	$13.2/11.5$	$0.491/0.582$	$0.486/0.539$
$\text{PWSS}b_1$	$\mathbf{13.3}/11.4$	$0.491/0.582$	$0.484/0.542$
B_2 [5]	$11.8/11.5$	$0.491/0.504$	$0.489/0.522$
$\text{PWSS}a_2$	$12.0/11.8$	$0.491/\mathbf{0.485}$	$0.488/0.484$
$\text{PWSS}b_2$	$11.9/11.9$	$0.494/0.524$	$0.487/0.508$

Table II shows no appreciable changes in the axial FWHM values relative to those listed in Table I, but the CNR and lateral FWHM values improve significantly in all cases, which illustrates the benefit of multi-angle coherent compounding. The best $\text{CNR}_{\text{Top}} = 13.3$ dB and $\text{CNR}_{\text{Bottom}} = 12.2$ dB are produced by $\text{PWSS}b_1$ and A, respectively. The second-best CNR_{Top} and $\text{CNR}_{\text{Bottom}}$ are due to $\text{PWSS}a_1$ (tied with B_1) and $\text{PWSS}b_2$, respectively. For the TYPE-1 images, $\text{PWSS}a_2$ offers the best $\text{FWHM}_{\text{Lateral}} = 0.485$ mm, followed by A (tied with B_2) giving the second-best lateral FWHM value. For the TYPE-2 images, A produces the best $\text{FWHM}_{\text{Lateral}} = 0.463$ mm, followed by $\text{PWSS}a_2$ offering the second-best lateral FWHM value.

According to Table II, our proposed methods PWSS*a* and PWSS*b* perform better than method B [5] in most cases. As mentioned earlier, PWSS*a* closely resembles B, except for a relatively small but important difference: PWSS*a* uses (7) for $\tau_\theta(z, x, p_x)$, whereas B uses

$$\tau_\theta(z, x, p_x) = p_x x + z\frac{1 + \cos(\theta)}{2c}\left[1 + \sqrt{1 - (cp_x)^2}\right], \quad (9)$$

which arises due to a slightly different modeling approach employed in [5].

Tables I and II show that both PWSS*a* and PWSS*b* give consistently better (e.g., up to 23% smaller) $\text{FWHM}_{\text{Lateral}}$ in comparison with DAS beamforming. While the latter gives better $\text{FWHM}_{\text{Axial}}$, the difference between the best and worst values is only 2% across all evaluated methods. On average, DAS beamforming and our slant-stack migration yield very similar CNR values (e.g., 12.2 dB vs. 12.1 dB in Table II).

IV. CONCLUSIONS

We have presented two plane-wave ultrasound image reconstruction methods, abbreviated as PWSS*a* and PWSS*b*, that are based on a geophysical slant-stack migration technique. Our evaluation results indicate that these methods generally outperform conventional DAS beamforming in terms of measured lateral FWHM values, and in some cases, giving better CNR values as well. The computational complexity of slant-stack migration is linearly dependent on the number of slants; however, using more slants does not necessarily improve the image quality (e.g., $\text{FWHM}_{\text{Lateral}}$ became better, but CNR_{Top} became worse). The main disadvantage of slant-stack migration is its inferior computational speed in comparison with frequency-wavenumber migration (e.g., methods A [5] and TM [12] mentioned in the previous section, as well as those reported in [8], [9], [11]). Further research in this area should investigate various opportunities for accelerating the execution of slant-stack migration and explore its extensions to plane-wave imaging of inhomogeneous media [13].

REFERENCES

[1] M. Tanter and M. Fink, "Ultrafast imaging in biomedical ultrasound," *IEEE Trans. Ultrason., Ferroelect., Freq. Contr.*, vol. 61, no. 1, pp. 102–119, Jan 2014.

[2] G. Montaldo, M. Tanter, J. Bercoff, N. Benech, and M. Fink, "Coherent plane-wave compounding for very high frame rate ultrasonography and transient elastography," *IEEE Trans. Ultrason., Ferroelect., Freq. Contr.*, vol. 56, no. 3, pp. 489–506, Mar 2009.

[3] O. Yilmaz, *Seismic Data Analysis*, 2nd ed. OK: SEG, 2001, vol. 1.

[4] J. Claerbout, *Imaging the Earth's Interior*. MA: Blackwell, 1985.

[5] M. Albulayli and D. Rakhmatov, "Fourier-domain depth migration for plane wave ultrasound imaging," *IEEE Trans. Ultrason., Ferroelect., Freq. Contr.*, vol. 65, no. 8, pp. 1321–1333, Aug 2018.

[6] CREATIS, "Plane-wave Imaging Challenge in Medical UltraSound (PICMUS): Algorithm Evaluation Framework." [Online]. Available: https://www.creatis.insa-lyon.fr/EvaluationPlatform/picmus/

[7] H. Liebgott, A. Rodriguez-Molares, F. Cervenansky, J. Jensen, and O. Bernard, "Plane-wave imaging challenge in medical ultrasound," in *Proc. IEEE International Ultrasonics Symposium*, Sep 2016, pp. 1–4.

[8] J. Cheng and J. Lu, "Extended high-frame rate imaging method with limited-diffraction beams," *IEEE Trans. Ultrason., Ferroelect., Freq. Contr.*, vol. 53, no. 5, pp. 880–899, May 2006.

[9] D. Garcia, L. Tarnec, S. Muth, E. Montagnon, J. Poree, and G. Cloutier, "Stolt's f-k migration for plane wave ultrasound imaging," *IEEE Trans. Ultrason., Ferroelect., Freq. Contr.*, vol. 60, no. 9, pp. 1853–1867, Sep 2013.

[10] A. Besson, M. Zhang, F. Varray, H. Liebgott, D. Friboulet, Y. Wiaux, J. Thiran, R. Carrillo, and O. Bernard, "A sparse reconstruction framework for Fourier-based plane-wave imaging," *IEEE Trans. Ultrason., Ferroelect., Freq. Contr.*, vol. 63, no. 12, pp. 2092–2106, Dec 2016.

[11] D. Liu and T. Ji, "Plane wave image formation in spatial-temporal frequency domain," in *Proc. IEEE International Ultrasonics Symposium*, Sep 2016, pp. 1–5.

[12] P. Temme and G. Mueller, "Fast plane-wave and single-shot migration by Fourier transform," *J. Geophys.*, vol. 60, pp. 19–27, 1986.

[13] D. Rakhmatov, "Stratified-medium plane-wave ultrasound image reconstruction via frequency-domain migration," in *Proc. IEEE International Symposium on Circuits and Systems*, May 2021, pp. 1–5.